29

Computational Techniques for Automotive Antenna Simulations

Faik Bogdanov[1,2], Roman Jobava[1,3], David Karkashadze[1,3], Paata Tsereteli[1], Anna Gheonjian[1], Ekaterina Yavolovskaya[1], Detlef Schleicher[4], Christoph Ullrich[5] and Hicham Tazi[5,6]

[1]*EM Consulting and Software, EMCoS Ltd., Tbilisi*
[2]*Georgian Technical University, Tbilisi*
[3]*Iv. Javakhishvili Tbilisi State University, Tbilisi*
[4]*VW AG, Wolfsburg*
[5]*AUDI AG, Ingolstadt*
[6]*Technische Universität München*
[1,2,3]*Georgia*
[4,5,6]*Germany*

1. Introduction

Automotive antenna design is a sophisticated process, related to both specific features of antennas itself, and their installation and operation in the complex electromagnetic (EM) environment of an automobile. Modern automobiles include a number of antenna solutions (AM/ FM radio, remote control systems, satellite services, etc.), operating simultaneously in the presence of car body, harness and electronic equipment. Design of them becomes even more complicated, when conformal and hidden antenna solutions are applied. These solutions encompass integrated glass antennas or active antennas, in combination with amplifiers, radio/ TV receivers and other network devices. Moreover, parametric tuning is required at all stages of development, making the complete chain of antenna design rather laborious and complex. These problems can be overcome using computer simulations with numerical analysis. However, accurate modelling of complicated models requires a combined usage of both traditional and special methods and techniques, including adaptive and hybrid ones, and special means for a fast and optimized numerical solution.

Though different computational methods are used, the Method of Moments (MoM) (Harrington, 1968) is the most popular method in automotive antenna design. This chapter describes the recent enhancements (Bogdanov & Jobava, 2003; Bogdanov et al. 2004a, Bogdanov et al., 2004b; Jobava et al., 2005; Bogdanov et al., 2009; Bogdanov et al., 2010a; Bogdanov et al., 2010b) of the traditional MoM, offering a set of up-to-date methods and techniques, whose application provides an accurate and effective solution of EM problems related to modern automotive antenna simulations. After description of methods or techniques, application examples are presented. These examples include comparisons to other methods and experimental data. All the calculations are performed using the MoM-based code "TriD" (Bogdanov et al., 2010c) being a core of the program packages "EMC Studio" (EMCoS, 2010a) and "EMCoS Antenna VirtualLab" (EMCoS, 2010b).

2. Traditional MoM

First, consider the traditional MoM applied to the boundary-value problem on geometry G (Harrington, 1993):

$$L(\vec{J}) = \vec{g} \tag{1}$$

where L is an integrodifferential operator, $\vec{g}$ is an excitation, and $\vec{J}$ is unknown current density on a given geometry G. Further, we discretize G to consider the following expansion for the unknown current:

$$\vec{J}(\vec{r}') = \sum_{n=1}^{N} I_n \vec{f}_n(\vec{r}') \tag{2}$$

where $\left\{\vec{f}_n(\vec{r}')\right\}_{n=1}^{N}$ are the expansion (basis) functions, I_n are unknown current coefficients, and N is the total number of unknowns dependent on the quality of discretization. Next, we substitute (2) into (1) and apply the testing procedure with weighting functions $\vec{w}_1(\vec{r}),...,\vec{w}_m(\vec{r}),...$ defined in the range of L to reduce (1) to a linear set of equations written as:

$$\mathbf{Z}^{MoM}\mathbf{I} = \mathbf{V} \tag{3}$$

where $\mathbf{Z}^{MoM}$ and $\mathbf{V}$ are, respectively, the MoM impedance matrix and voltage matrix-vector with elements $Z_{mn}^{MoM} = \left\langle \vec{w}_m, L\vec{f}_n \right\rangle$ and $V_m = \left\langle \vec{w}_m, \vec{g} \right\rangle$, and $\mathbf{I}$ is a vector of unknown coefficients I_n in the current expansion (2). Equation (3) defines the traditional MoM solution to the stated problem:

$$\mathbf{I} = (\mathbf{Z}^{MoM})^{-1}\mathbf{V} \tag{4}$$

3. Iterative MoM scheme for adaptive meshing

Analysis of (4) for the different discretizations of geometry G shows, that a uniformly fine mesh is not optimal enough to obtain a reasonably accurate solution. This section describes an iterative MoM scheme for generation of more optimal computational model. The scheme is based on analysis of an appropriate error metric for the solution. In each iteration step, the geometry is automatically re-discretized in a non-uniform way, until the best solution with a minimum number of unknowns is found.

Recent investigations (Bogdanov & Jobava, 2003; Bogdanov et al. 2004a, Bogdanov et al., 2004b; Jobava et al., 2005) show, that the accuracy of the MoM calculations can be controlled by estimation of the boundary conditions performance (BCP) on the scatterer surface S. Thus, a pair of BCP errors:

$$\varepsilon_E[\%] = 100\frac{\int_S |\vec{n}\times(\vec{E}^{sc}+\vec{E}^{inc})|\,dS}{\int_S |\vec{n}\times\vec{E}^{inc}|\,dS}, \quad \varepsilon_H[\%] \equiv 100\frac{\int_S |\vec{n}\cdot(\vec{H}^{sc}+\vec{H}^{inc})|\,dS}{\int_S |\vec{n}\times\vec{H}^{inc}|\,dS} \tag{5}$$

calculated for the total electric ($\vec{E}$) and magnetic ($\vec{H}$) fields, is sufficient enough to completely characterize the accuracy of the obtained MoM solution. Here, $\vec{n}$ is a normal to the scatterer

surface, and superscripts *inc* and *sc* denote the incident and scattered fields. Note, that the BCP error metric (4) is applicable to both closed and open surfaces providing the finite values of surface integrals and the proper normalization of error expressions. Besides, (4) directly indicates, how well the obtained solution satisfies the formulated problem. Also, the partial BCP errors may be considered to find the contribution of each geometry element to the total BCP error on the surface. Thus, the BCP error metric is the most convenient measure to estimate the accuracy of MoM solutions and build the adaptive iterative MoM scheme.
Fig. 1 shows a task flow for the iterative MoM scheme based on the analysis of the total and partial BCP errors on scatterer surface. This algorithm is working in hierarchical way.

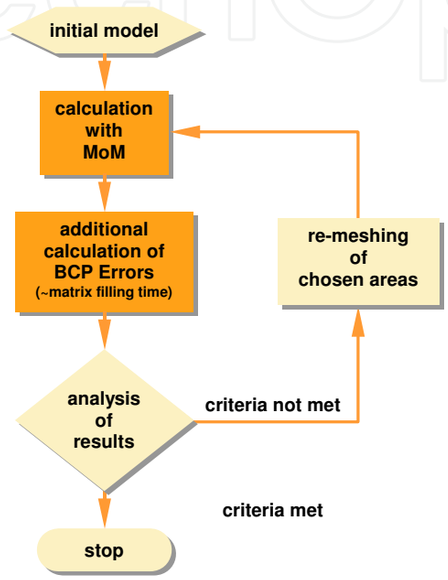

Fig. 1. Task flow for the BCP based adaptive iterative MoM scheme

First, MoM calculation for the initial "coarse" mesh is performed. Next, the BCP errors are calculated to estimate the solution accuracy and pick the geometry elements, which have contributed most strongly to the total BCP errors on the structure. After analysis of the BCP errors, further calculations are either stopped, or continued for the refined mesh, obtained after re-discretization of the chosen elements. The iterations are performed, till total BCP errors fall within a reasonable range.
The adaptive iterative scheme can be enhanced using the so-called *LSDM (Level-Surface-Difference-Minimum)* criteria (Jobava et al., 2005). After performing the initial calculation, the partial BCP errors are analyzed, so that all triangles with partial BCP errors higher than a prescribed value L (L-criterion) are considered as those for re-meshing. However, if the total area of triangles chosen for re-meshing is larger than a certain value $S\%$, in percentage to the total surface area (S-criterion), L-criterion is automatically enlarged, until the S-criterion is met. Further, a difference between the triangle areas chosen on the current and previous iterations is checked to be larger than a prescribed value $D\%$ (D-criterion). Finally, area of the chosen triangles is checked to be more than a prescribed value $M\%$, measured in percentage to the total surface area (M-criterion). If the previous criteria do not stop the iterations, re-meshing of the chosen areas and the further calculations are performed.
The adaptive iterative scheme has been verified on both closed and open geometries. Fig. 2 shows the total BCP errors on uniformly triangulated and adaptively meshed sphere

geometry. A sphere of radius R = 0.5 m is excited at a frequency f=300 MHz by a vertical electric dipole located at h = 0.02 m above the sphere surface to create a highly inhomogeneous incident near field. Fig. 2 illustrates a large advantage of the obtained adaptive meshes compared to the uniform mesh. Starting with a uniform mesh of 1,620 triangles and BCP errors of ε_E=55.4% and ε_H =21.8%, at the 2-nd iteration we obtain a mesh with 1,910 triangles and BCP errors of ε_E=17.40% and ε_H =11.1%. The same accuracy may be provided by a uniform mesh with 20,170 triangles (for BCP-E) and 20,720 triangles (for BCP-H). Compared to these uniform meshes, the calculation time for matrix inversion is lower by a factor of G_E=1,178, and G_H =1,277.

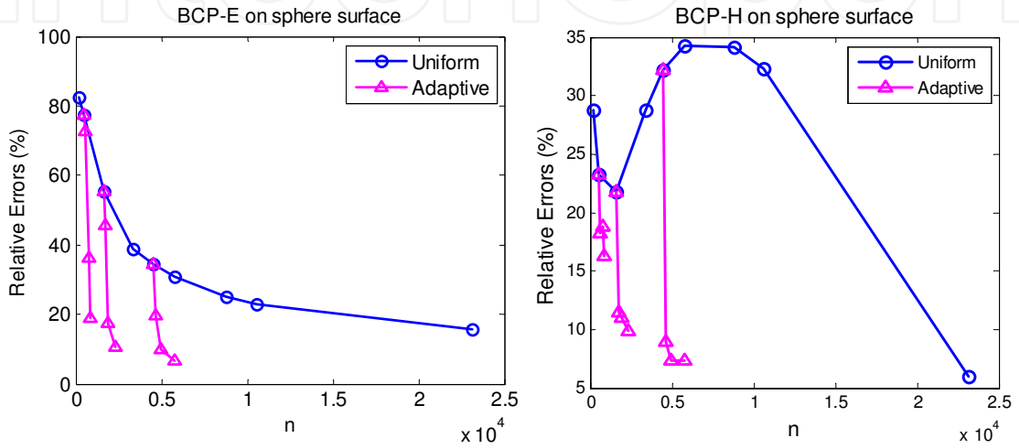

Fig. 2. Total BCP errors on a sphere surface for the uniform and adaptive meshes

Fig. 3 shows the adaptive meshes obtained for both closed (sphere) and open (square plate) geometries. The adaptive sphere mesh obtained at the 3-rd iteration consists of 2,342 triangles and is characterized by BCP errors ε_E=10.7% and ε_H =9.8%. Such accuracy cannot be achieved by any uniform mesh with less than 25,000 triangles. For the open geometry, 1-m plate is excited by a normally incident plane wave at frequency f = 300MHz. The adaptive plate mesh obtained at the 2nd iteration from an initial uniform mesh of 1,800 triangles, consists of 3,385 triangles and is characterized by the BCP errors ε_E=8.0% and ε_H =7.4%. Such accuracy cannot be achieved by a uniform mesh with less than 10,000 triangles.

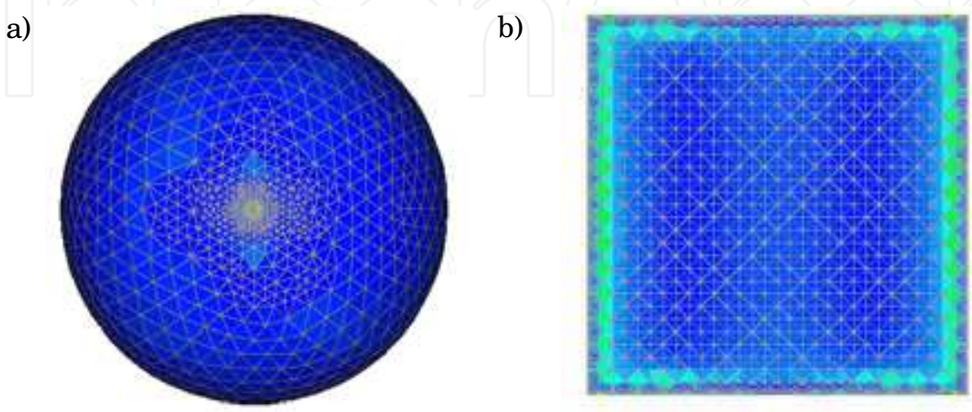

Fig. 3. The adaptive meshes: a) sphere geometry, b) plate geometry

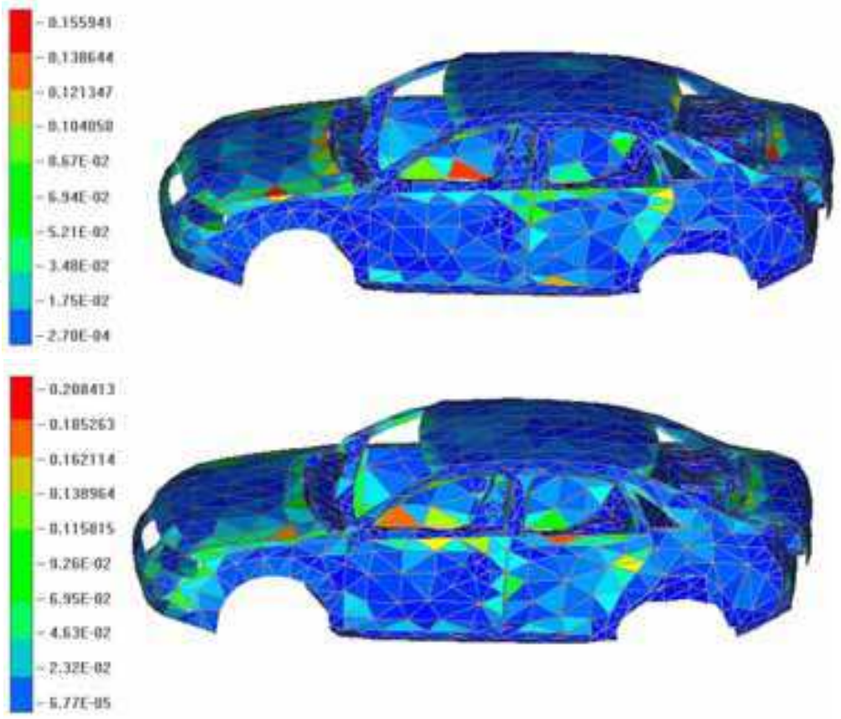

(a)

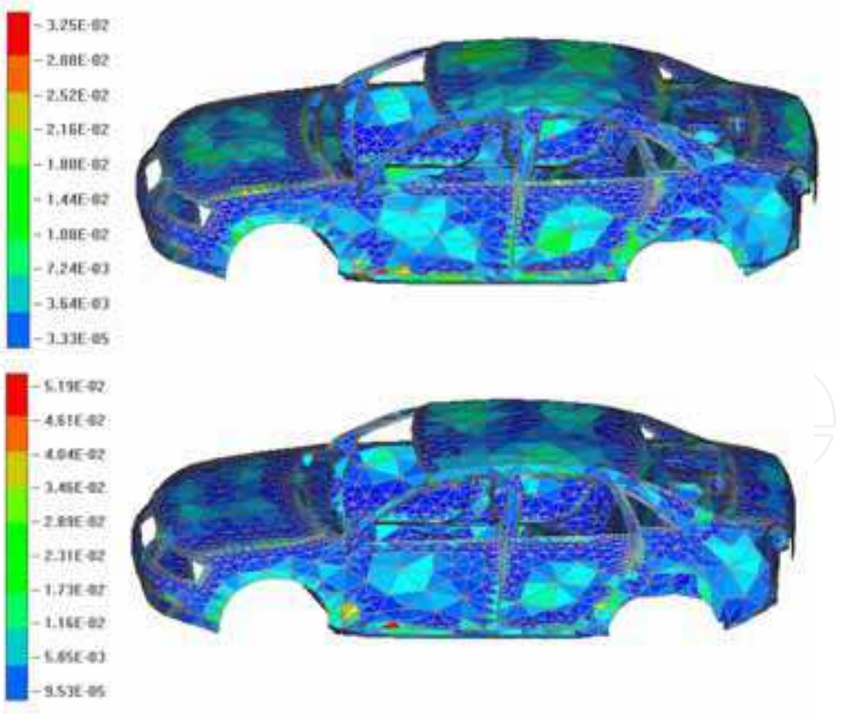

(b)

Fig. 4. BCP-E (top) and BCP-H (bottom) partial error distributions on: (a) initial car surface (4,449 triangles), (b) surface at iteration 2 (9,012 triangles)

Figs. 4 a) and b) present the distribution of partial BCP errors on initial and refined car model surfaces. It can be seen, that application of the suggested scheme leads to decrease of maximum partial errors. This results in more uniform distribution of partial BCP errors on the car surface.
So, at the 2-nd iteration, the maximum partial BCP errors on the car surface are decreased by 5 and 3.5 times for BCP-E and BCP-H errors, respectively. Such accuracy can be obtained by a uniform mesh with 13,340 triangles for BCP-E error and 14,550 triangles for BCP-H error.

4. Hybridization of MoM with multiport networks

4.1 Incorporation of network equations in the MoM

Modern automotive antennas frequently involve a number of network devices ("black boxes"), detailed analysis of which in the frame of MoM is either impossible, or unnecessary because of excessive computational intensity. This section describes a hybridization of the MoM with general multiport networks specified through their network parameters, such as open-circuit impedances (Z-matrices), short-circuit admittances (Y-matrices), scattering parameters (S-matrices), transmission lines (TL), etc.

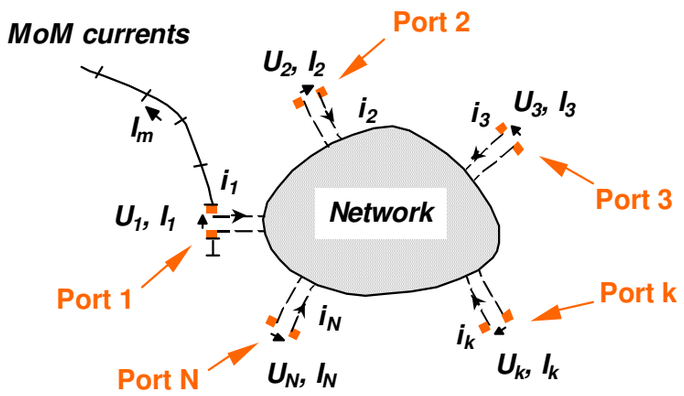

Fig. 5. N-port network directly connected to the MoM geometry

Fig. 5 shows a general N-port network connected to the wire segments, or ports of the MoM geometry. A network connection to the ports 1,2,...,N forces the currents $i_1, i_2,..., i_N$ through and voltages $U_1, U_2,..., U_N$ over the ports, according to the network parameters of the considered network.
Network parameters can be introduced via different forms of network equations:

$$\mathbf{U} = \mathbf{Z}^{Net}\mathbf{i} \tag{6a}$$

$$\mathbf{i} = \mathbf{Y}^{Net}\mathbf{U} \tag{6b}$$

$$\mathbf{a}^{-} = \mathbf{S}^{Net}\mathbf{a}^{+} \tag{6c}$$

where $\mathbf{i} = [i_1, i_2,..., i_N]$ and $\mathbf{U} = [U_1, U_2,..., U_N]$ are the network port current and voltage matrix-vectors, $\mathbf{Z}^{Net}$, $\mathbf{Y}^{Net}$ and $\mathbf{S}^{Net}$ are the network Z-, Y- and S-matrices with network parameters Z_{mn}^{Net}, Y_{mn}^{Net} and S_{mn}^{Net}; $\mathbf{a}^{\pm} = \frac{1}{2}\left(\bar{\mathbf{U}} \pm \bar{\mathbf{i}}\right)$ are normalized incident (+) and reflected

(-) port voltage vectors, $\bar{\mathbf{U}} = \mathbf{Z}_L^{-1/2}\mathbf{U}$ and $\bar{\mathbf{i}} = \mathbf{Z}_L^{1/2}\mathbf{i}$ are, respectively, normalized network voltage and current vectors, and $\mathbf{Z}_L$ is a diagonal matrix of characteristic impedances $Z_{L_1}, Z_{L_2}, ..., Z_{L_N}$ of transmission lines, connected to each port (reference impedances).
To incorporate the network equations (6a) to (6c) into the MoM system (3), it is necessary to relate the elements of matrix-vectors $\mathbf{V}$ and $\mathbf{I}$ in (3) to the network port voltage and current matrix-vectors $\mathbf{U}$ and $\mathbf{i}$. Let us choose the expansion and testing functions $\vec{f}_n(\vec{r}')$ and $\vec{w}_m(\vec{r}')$ in (2) and (3) so as to interpret V_m and I_n in (3) as segment currents and voltages. Then the segment voltages $\mathbf{V} = [V_1, \ldots V_m, \ldots]$ can be shared between those caused by external sources $\mathbf{V}^S = [V_1^s, \ldots V_m^s, \ldots]$ and those by network voltages $\mathbf{U} = [U_1, U_2, \ldots, U_N]$:

$$\mathbf{V} = \mathbf{V}^s + \mathbf{U} \tag{7}$$

For a free-port network (with controlled voltages), the port currents $\mathbf{i} = [i_1, i_2, \ldots, i_N]$ are easily related to the segment currents $\mathbf{I} = [I_1, I_2, \ldots, I_N]$:

$$\mathbf{i} = -\mathbf{I} \tag{8}$$

Therefore, inserting (8) in (6a) and then in (7) yields:

$$\mathbf{V} = \mathbf{V}^s - \mathbf{Z}^{Net}\mathbf{I} \tag{9}$$

Now introducing (9) in (3) and regrouping components with the currents $\mathbf{I}$ yields the following hybridized MoM and network algebraic system:

$$(\mathbf{Z}^{MoM} + \mathbf{Z}^{Net})\mathbf{I} = \mathbf{V}^s \tag{10}$$

For the mixed (free and forcing ports), the network equation (10) is generalized to:

$$(\mathbf{Z}^{MoM} + \mathbf{Z}'^{Net})\mathbf{I} = \mathbf{V}^s + \mathbf{V}^{add} \tag{11}$$

where $\mathbf{Z}'^{Net} = (\mathbf{Y}'^{Net})^{-1}$ is the free-port generalized impedance matrix of N-port network,

$$\mathbf{V}^{add} = -\mathbf{Z}'^{Net}\mathbf{Y}''^{Net}\mathbf{U}^S \tag{12}$$

is an additional voltage matrix-vector on free ports induced due to the connection to forcing ports, and $\mathbf{Y}'^{Net}$, $\mathbf{Y}''^{Net}$ are the free-port and mixed-port generalized network admittance matrices. The latter are mixed matrices with row index for the free port, and column index for the forcing port.
The matrix equations (11) represent the general hybridization of the MoM with multiport networks. Here, the total impedance matrix is composed of the MoM matrix and a reduced general network matrix for free ports, while the voltage column is composed of the MoM voltages and impressed network voltages, induced by the connection to the forcing ports. Specifically, for free-port network, (11) reduces to (10), while for the forcing-port network to (3), with $\mathbf{V} = \mathbf{V}^s$. In the latter case, the MoM system remains unchanged.

4.2 Validation of the hybrid MoM and network scheme

The derived hybrid MoM scheme is validated on a simple PSPICE model shown in Fig. 6. It consists of a 2-port linear amplifier network (outlined by the dashed line) connected to a 1-V voltage generator with internal resistance 50 Ω and loaded with a 1-m transmission line (TL)

with characteristic impedance 150 Ω and termination resistance *R*. The hybrid MoM simulation model is constructed of 4 wire segments to model the network ports (of S- and TL- types), 8 wire segments to model the excitation, connections and loads, and a frequency dependent S-matrix supplied by the PSPICE.

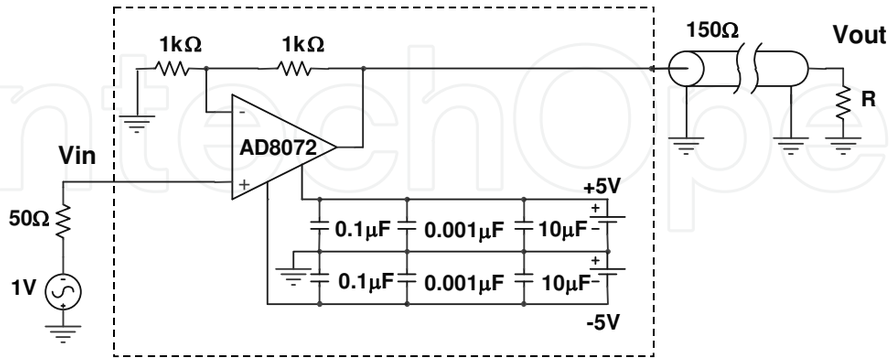

Fig. 6. Amplifier model with a transmission line

Fig. 7 shows a comparison of the transfer function calculated by hybrid MoM (TriD) and PSPICE (Su at al., 2008)

$$TF_V = V_{out} / V_{in} \tag{13}$$

where V_{out} is voltage on a transmission line termination, V_{in} is voltage at an amplifier input.

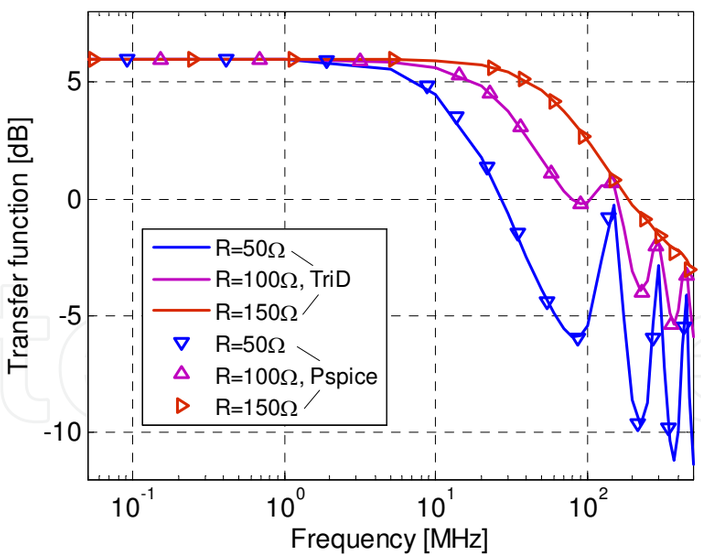

Fig. 7. Comparison of transfer functions calculated by the hybrid MoM (TriD) and PSPICE

The comparison of the TriD results with those calculated by PSPICE demonstrates a perfect agreement between them in a wide frequency range up to 500 MHz, including a flatness range up to 10 MHz, a smooth range for the matched termination resistance R = 150 Ω, and a high frequency oscillation range for the unmatched termination resistances R = 50 Ω and 100 Ω. These results validate the derived hybrid MoM and network scheme.

5. Hybridization of MoM with a special Green's function

5.1 Problem formulation

Modern automotive design tends towards conformal and hidden antenna applications, such as glass antennas integrated in vehicle windowpanes, as depicted in Fig. 8. An accurate MoM analysis of such antennas requires the discretization of the dielectric substrate of the glass, which results in an excessively large amount of unknowns (a several hundred of thousands). The usage of rigorous Green's functions of infinite layered geometries, represented by Sommerfeld integrals (Sommerfeld, 1949), is unfortunately too time-consuming and inflexible, whereas a frequently used approximate sheet impedance approximation (Harrington. & Mautz, 1975) fails for the complex glass antenna geometries (Bogdanov at al., 2010a). This section describes an equivalent glass antenna model of layered antenna structures and derives the hybrid MoM scheme, which incorporates the approximate Green's function of such a model.

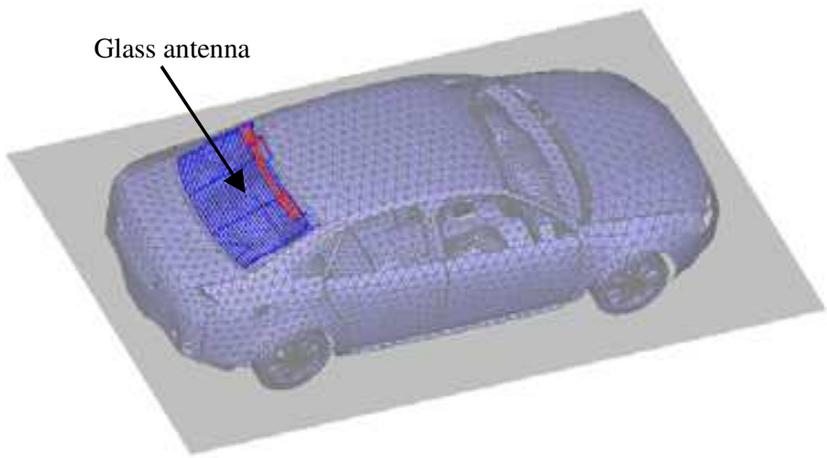

Fig. 8. Vehicle computational model with a glass antenna in the rear window

Let the total MoM geometry G of the considered problem be divided into basis (car) geometry B, glass antenna elements A and dielectric substrate D. The hybrid MoM formulation, excluding the dielectric geometry D from the consideration, can be written, instead of (1), as:

$$L(\vec{J}^B) + L_G(\vec{J}^A) = \vec{g}^B + \vec{g}_G^A \text{ on } S^B \tag{14a}$$

$$L_G(\vec{J}^B) + L_G(\vec{J}^A) = \vec{g}_G^B + \vec{g}_G^A \text{ on } S^A \tag{14b}$$

where the superscripts B and A stand for the basis and glass antenna elements, and L_G and $\vec{g}_G$ are the boundary operator and excitation modified so as to include the dielectric effect and automatically satisfy boundary conditions on the dielectric. To derive the hybrid MoM scheme and define the operators L_G and $\vec{g}_G$, consider an equivalent glass antenna model, allowing construction of approximate Green's function for the layered antenna structures.

5.2 Equivalent glass antenna model

Fig. 9 a) shows an original structure of the metallic strip (glass antenna element) A with current $\vec{J}$ placed above, inside or under the dielectric layer (regions i=1,2,3, respectively).

The layer of thickness l and material parameters ε_0, μ_0 (region i=2) is placed in vacuum with parameters ε_0, μ_0 (i=1,3). In a multilayer case, effective material parameters are considered.

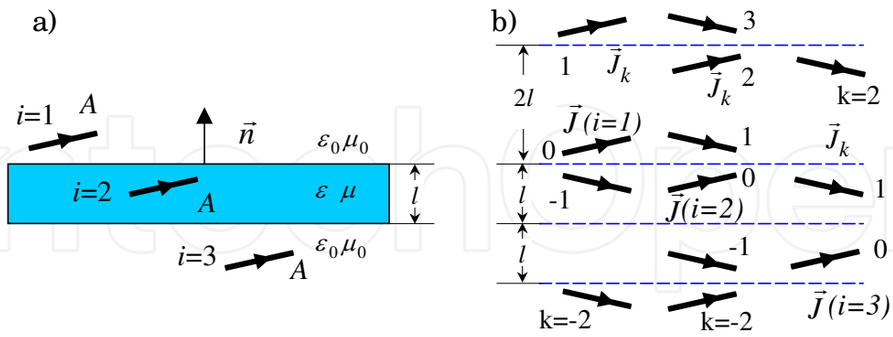

Fig. 9. a) Original and b) equivalent glass antenna model

Fig. 9 b) shows an equivalent model of microstrip structure in Fig. 2 a) consisting of the source current $\vec{J}$ on element A and its mirror images $\vec{J}_k$ ($k = 0,\pm1,\pm2,...$) in top and bottom dielectric layer interfaces. For the source current $\vec{J}$ in the region i, an electromagnetic field at the observation region j=1,2,3 is composed of the field of the original current $\vec{J}$ (if only j=i) and that produced by its images $\vec{J}_k$ taken with amplitudes A_{kv}^{ji} and A_{kh}^{ji} for the vertical and horizontal components of the vector potentials, and A_{kq}^{ji} for the scalar potentials. Hereinafter, the 1-st superscript indicates the observation region, and the 2nd the source region.

Note, that both the source and image currents, radiate in medium with material properties of the observation region j, and only images, which are not placed in the observation region, radiate into this region. The image amplitudes A_{kt}^{ji}, $t = v,h,q$ can be approximately found by recursive application of the mirror image method to relate these amplitudes with those (a_t^{ji}) obtained for the approximate solution of the boundary-value problem on a separate dielectric interface.

5.3 Derivation of image amplitudes

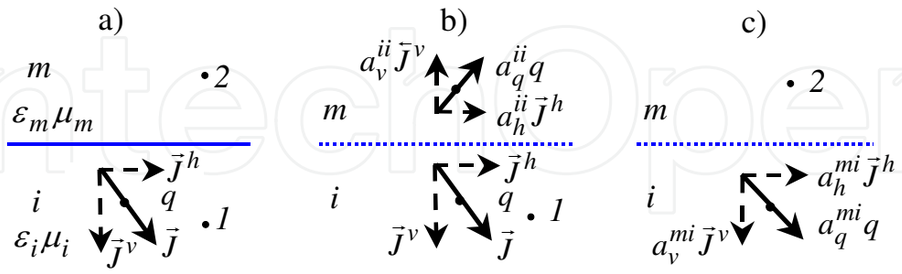

Fig. 10. Sources and images in the presence of dielectric interface: a) original problem, b) equivalent problem for the source region i, c) equivalent problem for the mirror region m

In order to find the image amplitudes a_t^{ji}, let's place the current $\vec{J}$ and the associated charge $q = \mp\frac{1}{i\omega}\mathrm{div}\,\vec{J}HV$ from one side (for instance, in medium i) of the interface between the two dielectric media m and i, as depicted in Fig. 10 a). Following the modified image theory (MIT) (Miller et al., 1972a; Ala & Di Silvestre, 2002), an electromagnetic response from the imperfect interface is approximately described by inserting the mirror image source

radiating to the source region i, and the space-like image source radiating to the mirror region m, see Figs. 10 b) to c). The original current $\vec{J}$ is decomposed into its vertical $\vec{J}^v$ and horizontal $\vec{J}^h$ components, and $\vec{J}^v = -\vec{J}^v$. Unlike the canonical mirror image method, image amplitudes α_t^{ji} are modified so as to approximately satisfy the boundary conditions.

Unlike other MIT applications, we reconsider the derivation of image amplitudes α_t^{ji}, imposing boundary conditions on both electric and magnetic fields and applying the quasi-static approximation $(kR)^2 << 1$, where k is a wavenumber, and R is a distance between the image and observation points. Besides, we assign the different amplitudes α_v^{ji}, α_h^{ji} and α_q^{ji} for the current and charge images, in view of nonuniqueness of vector and scalar potentials in the presence of a dielectric boundary (Erteza & Park, 1969). This results in the following approximate solution to Sommerfeld problem in Figs. 10 b) and c) (Bogdanov et al., 2010b):

$$\alpha_q^{ii} = \alpha_v^{ii} = \frac{\varepsilon_i - \varepsilon_m}{\varepsilon_i + \varepsilon_m}, \qquad \alpha_q^{mi} = \alpha_v^{mi} = \frac{2\varepsilon_m}{\varepsilon_i + \varepsilon_m} \tag{15a}$$

$$\alpha_h^{ii} = \frac{\mu_m - \mu_i}{\mu_i + \mu_m}, \qquad \alpha_h^{mi} = \frac{2\mu_i}{\mu_i + \mu_m} \tag{15b}$$

Once the image amplitudes α_t^{ji} of the equivalent interface problem are found, we develop a recursive procedure (Bogdanov et al., 2010b) to derive the image amplitudes A_{kt}^{ji} of the equivalent glass antenna problem in Fig. 9 b). Let us derive it for the source current $\vec{J}$ situated in the region i=1 (above the layer). To satisfy boundary conditions on the upper dielectric interface, we introduce, along with source current $\vec{J}$ radiating in the source region 1, two image currents located on equal distances d from the interface: mirror current $\vec{J}_{-1}$ with amplitude $A_{-1t}^{11} = \alpha_t^{11}$, again radiating in region 1, and space-like image $\vec{J}_0$ with amplitude $A_{0t}^{21} = \alpha_t^{21}$ radiating in region 2. The same procedure for the image current $\vec{J}_0$ radiating in region 2 in the presence of the bottom interface, requires a pair of additional image currents located at equal distances $l + d$ from this interface: $\vec{J}_{-2}$ with amplitude $A_{-2t}^{21} = \alpha_t^{21}\alpha_t^{22}$ radiating in region 2, and $\vec{J}_0$ with amplitude $A_{0t}^{31} = \alpha_t^{21}\alpha_t^{12}$ radiating in region 3. Next, we should adjust the boundary conditions on the upper interface, which are unbalanced due to the radiation of image current $\vec{J}_{-2}$ with amplitude $\alpha_t^{21}\alpha_t^{22}$ in region 2 in the presence of the upper interface. Recursively continuing this procedure results in:

$$A_{-1t}^{11} = \alpha_t^{11}; \quad A_{-kt}^{11} = \alpha_t^{21}\alpha_t^{12}(\alpha_t^{22})^{2k-3}, \quad A_{-kt}^{21} = \alpha_t^{21}(\alpha_t^{22})^{2k-3}, \quad k = 2,3,... \tag{16a}$$

$$A_{kt}^{21} = \alpha_t^{21}(\alpha_t^{22})^{2k}, \qquad A_{kt}^{31} = \alpha_t^{21}\alpha_t^{12}(\alpha_t^{22})^{2k}, \qquad k = 0,1,2,... \tag{16b}$$

5.4 MoM Solution to the equivalent glass antenna model

The equivalent glass antenna model in Fig. 9 b) allows to introduce the equivalent current and charge associated with antenna element A into any observation region j=1,2,3:

$$\vec{J} = \vec{J}\delta_{ij} + \sum_k [A_{kv}^{ji}\vec{J}_k^v + A_{kh}^{ji}\vec{J}_k^h] \tag{17}$$

$$i/\omega\,\nabla\vec{J} = i/\omega\,(\nabla\vec{J}\delta_{ij} + \sum_k A_{kq}^{ji}\nabla\vec{J}_k) \tag{17a}$$

where $\vec{J}$ is the original current in the i-th region, δ_{ij} is the Kronecker delta, $\vec{J}_k = \Re_k \vec{J}$ is the current on the k-th image, $\Re_k$ is the imaging operator, $\vec{J}_k^v = (\vec{J}_k \hat{n})\hat{n}$ and $\vec{J}_k^h = \vec{J}_k - \vec{J}_k^v$ are the vertical and horizontal components of the k-th image currents, and $\hat{n}$ is a unit normal vector to the dielectric interface. Since (17) can be considered as $\vec{J} = \Im(\vec{J})$, where $\Im$ is a transforming operator, and modifying the excitation $\vec{g}' = \Im(\vec{g})$, after substitution in (1), we arrive at the following equivalent boundary-value problem on antenna element geometry A:

$$L_G(\vec{J}) = \vec{g}_G \tag{18}$$

where:

$$L_G = L\Im\,,\ \vec{g}_G = \Im\vec{g} \tag{19}$$

are the modified boundary operator and excitation in the glass area including the dielectric effect. Equation (18) allows to obtain the MoM solution to the glass antenna problem, applying the traditional MoM scheme of Section 2 to the equivalent model in Fig. 9 b) with expansion functions taken on both original and image geometries, and testing only on the original geometry.

5.5 Hybrid MoM scheme with incorporated equivalent glass antenna model

Expression (19) allows to reduce the hybrid MoM formulation (14) to a linear set of algebraic equations. Applying the traditional MoM scheme of Section 2 with expansion functions $\left\{\vec{f}_n(\vec{r}')\right\}_{n=1}^{N}$ and weighting functions $\{\vec{w}_m(\vec{r})\}_{m=1}^{N}$ results in the following matrix equations:

$$\begin{bmatrix} [Z_{mn}^{BB}] & [Z_{mn}'^{BA}] \\ [Z_{mn}'^{AB}] & [Z_{mn}'^{AA}] \end{bmatrix} \begin{bmatrix} [I_n^B] \\ [I_n^A] \end{bmatrix} = \begin{bmatrix} [V_m^{BB}] + [V_m'^{BA}] \\ [V_m'^{AB}] + [V_m'^{AA}] \end{bmatrix} \tag{20}$$

where $Z_{mn}^{BB} = \left\langle \vec{w}_m^B, L\vec{f}_n^B \right\rangle$ $Z_{mn}'^{\beta\alpha} = \left\langle \vec{w}_m^\beta, L_G \vec{f}_n^\alpha \right\rangle$ are the MoM impedance matrix elements, $V_m^{BB} = \left\langle \vec{w}_m^B, \vec{g}^B \right\rangle$, $V_m'^{\beta\alpha} = \left\langle \vec{w}_m^\beta, \vec{g}_G^\alpha \right\rangle$ the excitation elements, and $\alpha, \beta = \{A, B\}$. The linear set (20) incorporates the equivalent glass antenna model into the full MoM geometry.

Note, that although equivalent glass antenna model is derived for infinite dielectric layers, it also can approximately be applied to finitely sized and even slightly curved glass antenna geometries. For this purpose, a finite-size dielectric substrate is subdivided into separate flat areas, and each antenna element is associated with the closest glass area. The antenna elements near this area are considered to radiate as located in the presence of infinite dielectric substrate being the extension of this smaller glass area.

5.6 Application of hybrid MoM scheme with incorporated equivalent glass antenna

The derived hybrid MoM scheme has been applied to simulate reflection coefficient of rear window glass antenna in full car model. Results were compared with measurements.

A simulation model of the measurement setup with glass antenna and its AM/ FM1/ TV1 port is shown in Fig. 11. This model consists of 19,052 metal triangles to model the car bodyshell, 67 wire segments to model the antenna to body connections, and 2,477 triangles to model the glass antenna elements, giving a total of N = 31,028 unknowns. The curved glass surface is represented by 5,210 triangles. The dielectric substrate is of thickness l = 3.14 mm, relative permittivity ε_r = 7.5, and dielectric loss tangent tan (δ) = 0.02. The metallic elements are assumed to be perfectly conducting. To accurately represent measurement

setup, BNC connectors attached to the antenna terminals. The connectors are modelled as non-radiating TL elements of 64-mm length and 50-Ohm characteristic impedance.
Fig. 12 shows measured and simulated results for the reflection coefficient $|S_{11}|$ at the FM1 port of the glass antenna. Comparison between these results shows that simulated results are in a close agreement with measurement data at all frequencies in the range from 30 to 300 MHz.

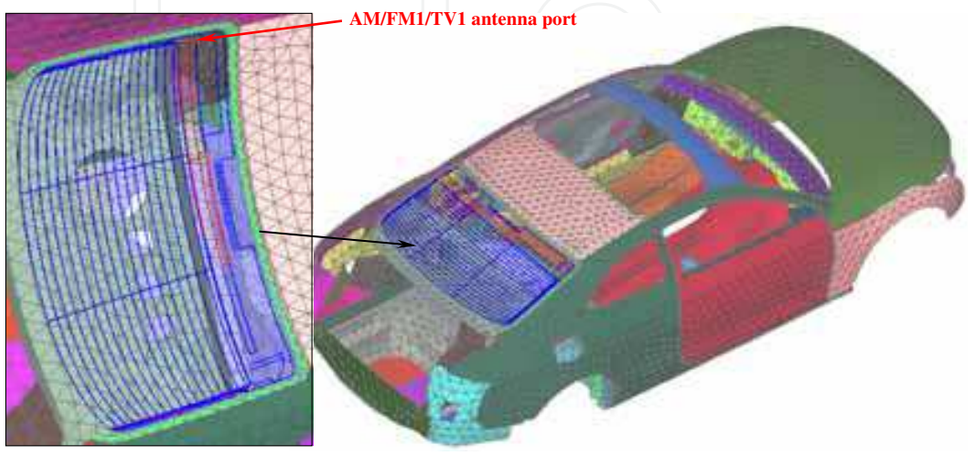

Fig. 11. A simulation model of the measurement setup with the glass antenna with FM port

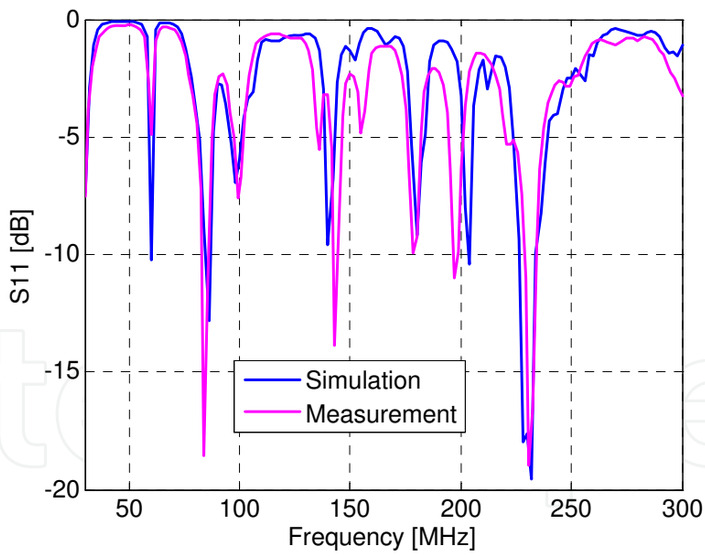

Fig. 12. Comparison of measurement and simulation results for a full car model

6. Multi-partitioned and multi-excitation MoM scheme

6.1 Problem formulation

In the optimization of automotive antenna, a considerable part of the vehicle geometry remains the same in different calculations. For instance, this happens when one compares characteristics of different antennas mounted in a windowpane of the same car model. This

also happens when optimizing the shape, dimensions, position and material parameters of certain antenna installed in the vehicle. Besides, an optimization of the calculation procedure for different sets of excitations is required. This section describes a multi-partitioned and multi-excitation MoM scheme to effectively handle such geometries and excitations.

Let G be a series of geometries $G_1, G_2, ..., G_K$ with a predominant common (basis) part $G^b = \bigcap_{k=1}^{K} G_k$ being an intersection of the geometries G_k. The analysis of the geometries G_k, $k = 1, 2, ...K$ using the traditional MoM scheme of section 2 requires CPU time that K times exceeds that needed to handle a single geometry. Our intention is to enhance the MoM scheme in such a way as to essentially minimize the total CPU time needed to handle a series of geometries under different sets of excitations.

6.2 Partitioned MoM scheme

Let geometry G_k be partitioned on the basis G^b and additional G^a parts, so that $G_k = G^b + G^a$. Reconsidering the boundary-value problem (1) with applying the partitioned sets of expansion and testing functions for the basis G^b and additional G^a geometries, we reduce (1) to the matrix equations with the following block structure:

$$\begin{bmatrix} Z^{bb} & Z^{ba} \\ Z^{ab} & Z^{aa} \end{bmatrix} \begin{bmatrix} I^b \\ I^a \end{bmatrix} = \begin{bmatrix} V^b \\ V^a \end{bmatrix} \tag{21}$$

where the first superscript is associated with the testing procedure, and the second one with the expansion procedure, so that the total number of unknowns is $N = N^b + N^a$.

Considering now the LU decomposition of the partitioned impedance matrix:

$$\begin{bmatrix} Z^{bb} & Z^{ba} \\ Z^{ab} & Z^{aa} \end{bmatrix} = \begin{bmatrix} L^{bb} & 0 \\ L^{ab} & L^{aa} \end{bmatrix} \begin{bmatrix} U^{bb} & U^{ba} \\ 0 & U^{aa} \end{bmatrix} \tag{22}$$

one can see that the decomposition of the basis block matrix $Z^{bb} = L^{bb}U^{bb}$ is the same as the one which would be obtained for the basis geometry G^b. Therefore, considering first the boundary-value problem on the basis geometry G^b and storing the inverted matrices $\breve{L}^{bb} = (L^{bb})^{-1}$ and $\breve{U}^{bb} = (U^{bb})^{-1}$ for this geometry, one then only needs to calculate the additional blocks of the partitioned impedance matrix in (21) to determine the additional blocks in the LU decomposition (22). Then, the solution of the initial boundary-value problem on the total geometry G_k is found to be:

$$\begin{bmatrix} I^b \\ I^a \end{bmatrix} = \begin{bmatrix} U^{bb} & U^{ba} \\ 0 & U^{aa} \end{bmatrix}^{-1} \begin{bmatrix} L^{bb} & 0 \\ L^{ab} & L^{aa} \end{bmatrix}^{-1} \begin{bmatrix} V^b \\ V^a \end{bmatrix} \tag{23}$$

or, after inversion of block matrices

$$\begin{bmatrix} I^b \\ I^a \end{bmatrix} = \begin{bmatrix} \breve{U}^{bb} & \tilde{U}^{ba} \\ 0 & \breve{U}^{aa} \end{bmatrix} \begin{bmatrix} \breve{L}^{bb} & 0 \\ \tilde{L}^{ab} & \breve{L}^{aa} \end{bmatrix} \begin{bmatrix} V^b \\ V^a \end{bmatrix} \tag{24}$$

where $\tilde{U}^{ba} = -(\breve{U}^{bb}\, U^{ba})\, \breve{U}^{aa}$, $\tilde{L}^{ab} = -(\breve{L}^{aa}\, L^{ba})\, \breve{L}^{bb}$. In (24), a predominant part of the calculations is associated with determining the inverse block matrices $\breve{L}^{bb}$ and $\breve{U}^{bb}$ for the basis geometry G^b to be stored at the first stage of calculations. If the additional part G^a of the total geometry G_k is much less than the basis part G^b, the calculation of additional blocks needs far fewer operations than those required for the total geometry. This allows performing the additional calculations to obtain the sought solution without considerable usage of CPU time. The structure of multi-partitioned and multi-excitation calculations is illustrated in Fig. 13.

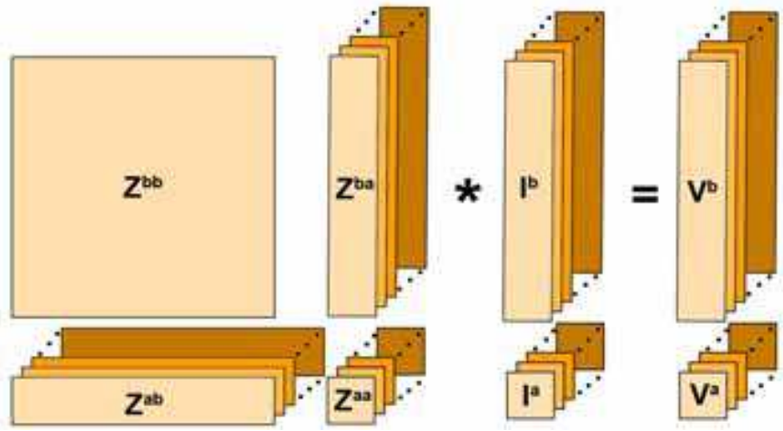

Fig. 13. Structure of multi-partitioned and multi-excitation calculations

A theoretical gain in solving time obtained when applying the partitioned MoM scheme (if using the stored LU matrices for the basis geometry) may be evaluated as:

$$G = \frac{1}{(1-\beta)/\ K + \beta} \tag{25}$$

where $K = 1/\ [1-(1-\alpha)^3]$ is a theoretical gain of LU decomposition, $\alpha = N^a / (N^b + N^a)$ is a share of additional unknowns in a total number of unknowns, and β is a share of the additional time in a direct task time, which is necessary for the calculation processing (this is characterized by the computational system). This time includes the needed data preparation, loops and threads organization, memory access, etc. For in-core calculations, this time may be ignored, while for out-of-core calculations it should include HDD read/ write time, and for the cluster (distributed memory) calculations it should include the data exchange time (the latter time may be rather significant to appreciably reduce the estimation gain).

Tables 1 and 2 compare the solving times and gains for the sequential/ multithreaded and cluster calculations. These tasks have been run on 2CPU Intel Xeon 3.00 GHz computers (totally 4 cores); and the cluster consists of the 9 computers (altogether 36 processes).

N^b	N^a	α	$G \equiv K$	**1 thread used**		**4 threads used**	
				Direct [s]	Partition [s]	Direct [s]	Partition [s]
28093	2935	0.095	3.87	8063	2116	2233	750
28093	118	0.004	80.03	6052	91	1696	38

Table 1. Solving times and gains for sequential calculations for $\beta = 0$.

N^b	N^a	α	K	Direct [s]		β	G	**Partition** [s]
				Solve	Exchange			Solve
28093	2935	0.095	3.87	474	200	0.42	1.75	332
28093	118	0.004	80.03	383	170	0.44	2.22	211

Table 2. Solving times and gains for cluster calculations.

The presented data shows the sufficient advantage of using the partitioned MoM scheme when applied to a series of partitioned geometries with a predominant basis part (small values of α). However, this scheme is less effective in the case of distributed memory (parallel) calculations, because of a large amount of data exchange (even theoretically, it cannot be more than $1/\beta$). Optimizing the data exchange in the multi-partitioned regime, one can significantly decrease the average β, which results in increase of the gain.

6.3 Application of the multi-partitioned MoM scheme

The derived multi-partitioned MoM scheme has been applied to optimize glass antenna structure in a full car model. Fig. 14 shows a computational model of AUDI A5 with a heating structure and antenna pattern printed on the rear windscreen. A part of the antenna structure used for AM, FM and TV services, is to be optimised (this part is electrically separated from the heating structure and therefore may be easily changed during the antenna design).

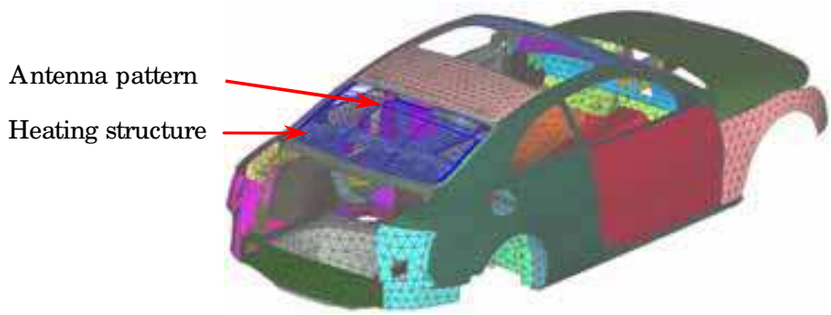

Fig. 14. AUDI A5 car body with heating structure printed on rear windscreen

In using the multi-partitioned scheme, we consider the car bodyshell and the heating structure as a basis part of geometry (altogether 20,573 metallic elements), and the antenna structure as additional (partition) part. Figs. 15 a) to c) show different variants of the antenna structure with a corresponding pigtail wire, which are considered as partitions. Fig. 15 d) compares the reflection coefficients of the full car models with the above antenna variants, calculated in the frequency range from 30 MHz to 300 MHz. The obtained results show that modification of the antenna structure do not change the reflection coefficient in the FM frequency range, but significantly shifts and change the level of resonances in the TV range (150-175 MHz and 210-225 MHz).

Table 3 compares the computational times needed for calculation of 3 variants of the antenna structure using the direct MoM respectively the multi-partitioned approach. Comparison of CPU times shows 1.5 gain in calculation time for 3 partitions that demonstrates advantage of the multi-partitioned scheme to solve optimization problems on full car models. It should also be mentioned that the benefit of the multi-partitioned

approach increases if more variants are to be compared. This is quite often the case in early stages of development when many different antenna positions and layouts are still viable.

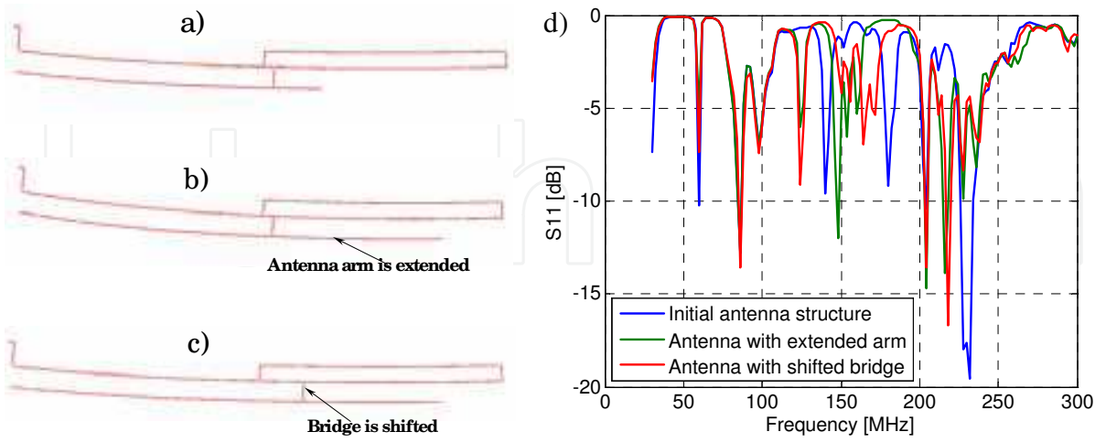

Fig. 15. Different variants of the antenna structure: a) initial structure, 102 metallic elements, b) structure with extended arm, 117 metallic elements, c) structure with shifted bridge, 117 metallic elements, d) reflection coefficient of above antennas as a function of frequency

Solution type	CPU time for one frequency point
Direct solution (3 tasks)	3.7 hours (1.23 hours per task)
Matrix partitioned approach (3 partitions)	2.55 hours (1.9 hours for basis + 0.65 hours for 3 partitions; 13 minutes for each partition)

Table 3. Summary of computational times

7. Application of computational techniques to automotive EM problems

7.1 Simulations of vehicle antenna validation tests

The developed techniques have been applied to simulate various EM and EMC (Electromagnetic Compatibility) problems on automotive antennas.

First, a vehicle antenna validation test (usually, it precedes a chamber vehicle emission test) is modelled. A schematic representation of this test is shown in Fig. 16.

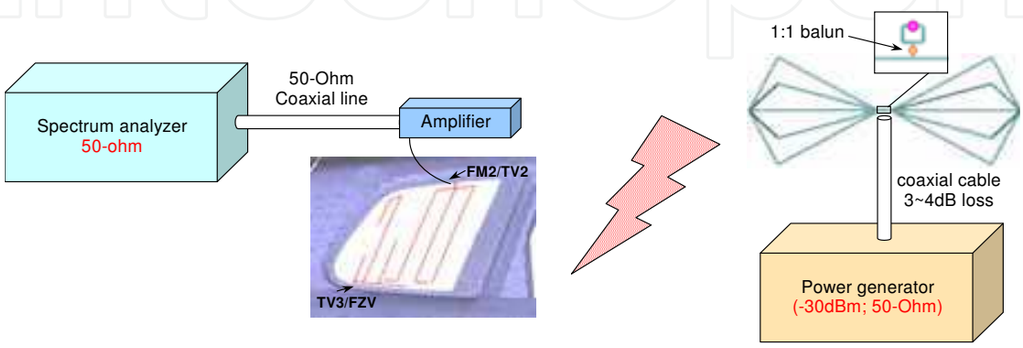

Fig. 16. Schematic representation of antenna validation test

A measurement setup consists of active vehicle antenna (with amplifier) exposed by a test antenna with defined feeding, and a spectrum analyzer to measure the coupled voltage. The obtained voltage level is compared to the standard acceptable reception level, known for each type of vehicle antenna. The computer simulations are aimed to predict the total antenna system performance in order to detect possible problems, especially if a real car prototype is not yet available for measurements. Fig. 17 shows used mutual location of the car and test antennas in an anechoic chamber.

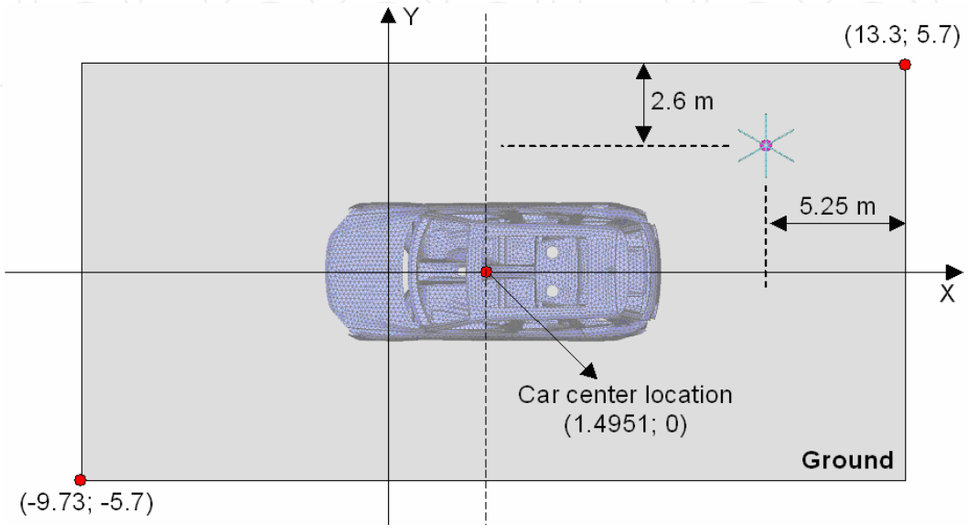

Fig. 17. Mutual location of the car and test antenna in anechoic chamber

In a current example, a vertically polarized biconical SCHWARZBECK BBA9106 test antenna with 1:1 balun is used. The antenna located at 1.0 m above the ground is fed by a -30dBm generator with 50-Ohm internal resistance, connected to the antenna by a lossy coaxial cable. The dimensions and antenna factor of the test antenna are presented in Figs. 18 and 19.

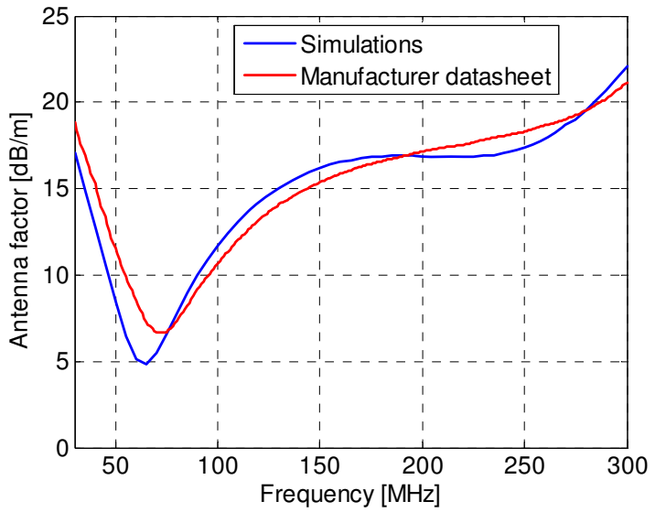

Fig. 18. Antenna factor

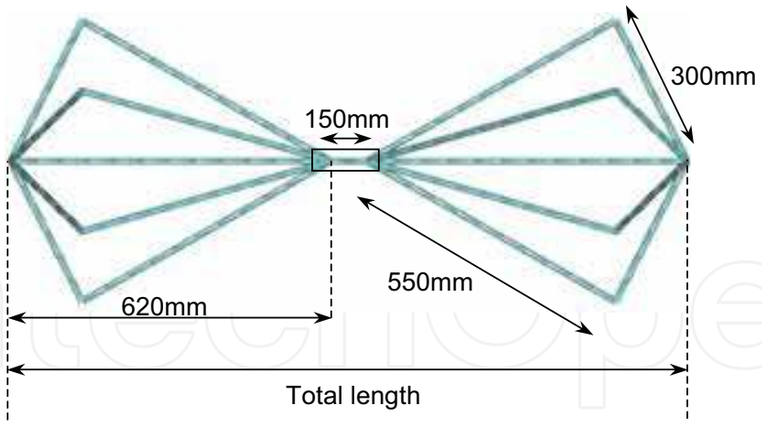

Fig. 19. Test antenna dimensions

A simulation model of the side window TV2 antenna in a VW car is shown in Fig. 20. It consists of 31,045 triangles to model the car bodyshell, and 535 triangles and 19 wire segments to model the antenna pattern. The antenna pattern is printed on the right rear window glass of thickness l =3 mm, permittivity ε_r=7, loss tangent tan (δ)=0.02, and is adjacent to the TV3/ FZV antenna.

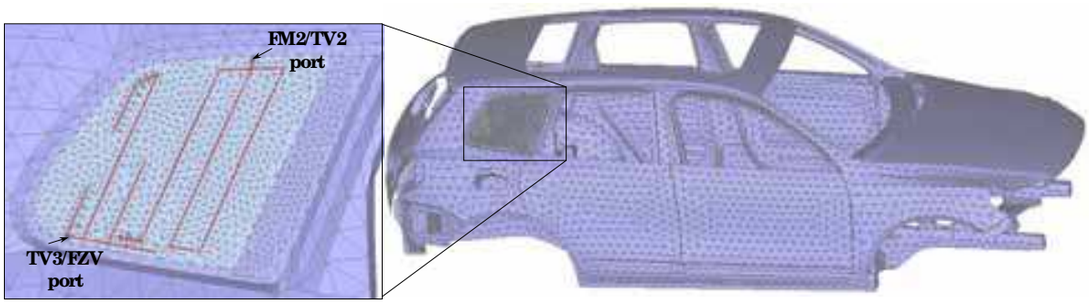

Fig. 20. VW car model with glass antenna in right window

To properly model the validation test, the antenna amplifiers are also included in the simulation model as non-radiating networks. The scattering parameters of the TV2 and TV3 antenna amplifiers are depicted in Figs. 21 a) and b). It is assumed, that a backward transmission of the signal from radio to antenna pattern is negligibly small, and that the amplifier output is perfectly matched with a 50-Ohm coaxial cable connected to radio. Thus, a complete simulation model consists of the biconical test antenna, car bodyshell model and side window glass antenna with amplifiers. The analysis of such a model requires the following modelling techniques: power normalization of the biconical antenna source, hybridization of the MoM with special Green's function to model the glass antenna, and hybridization of the MoM with multiport networks to model the amplifiers and lossy coaxial cables.

Fig. 22 shows the comparison of the simulated voltage at TV2 amplifier output port with measurement results obtained in Volkswagen AG. Two separate frequency ranges are considered: 40 MHz - 110 MHz (Bands I and II), and 170 MHz -230 MHz (Band III).

Comparison of the simulated results with measurements shows a rather good agreement between them in both TV1 and TV2 frequency ranges. The maximum difference between coupled voltages does not exceed 6 dB.

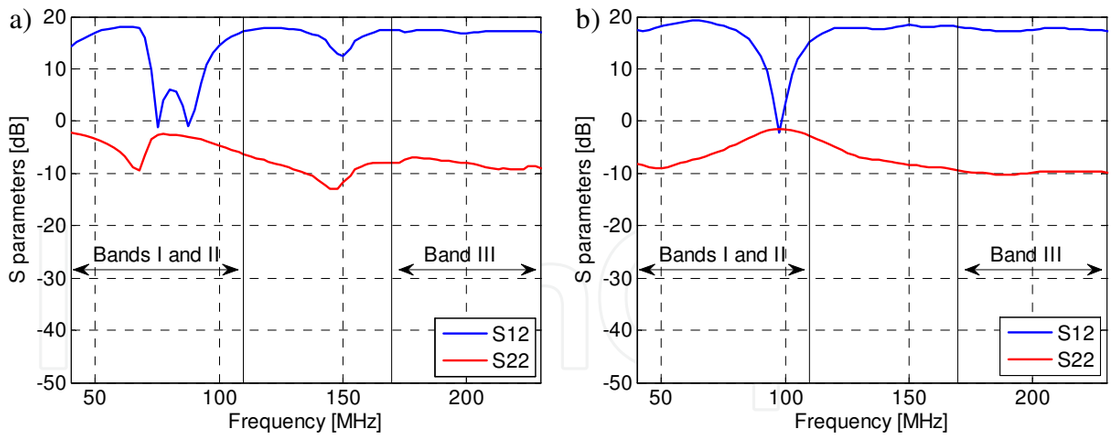

Fig. 21. S-parameters of: a) TV2 amplifier, b) TV3 amplifier

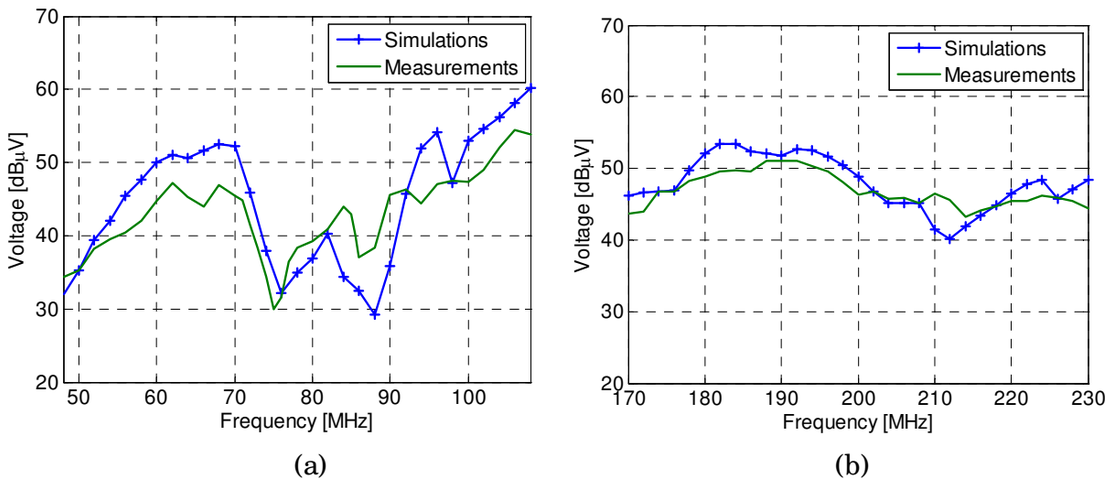

Fig. 22. Voltage received by TV2 antenna in: a) Band I and II, b) Band III

7.2 Testing of vehicle antenna reception in an open-area far-field test setup

Next, a vehicle antenna reception in an open-area far-field test setup is modelled. Examination of vehicle antenna reception is one of the stages in system development and certification. A single-axis rotational technique is used to measure the antenna reception pattern. This technique involves placing the equipment under test on a rotational positioner and rotating about the azimuth to measure a two-dimensional polar pattern. It is important to be able to measure two perpendicular (vertical and horizontal) components of pattern. This measurement is usually accomplished by using a dual-polarized horn, log-periodic dipole array, or dipole antenna as the transmitting antenna and requires two transmitters or the ability to automatically switch the polarization of a single transmitter. A typical polar-pattern test setup is shown in Fig. 23.

The vehicle with antenna under test (AUT) is placed on a rotating turntable; transmitting antenna is placed at a certain level above ground and at fixed distance away from the AUT. The turntable is rotated over 360°, and the response between the antennas is measured as a function of angle. A distance between the transmitting antenna and AUT is taken to be large enough to satisfy far-field condition.

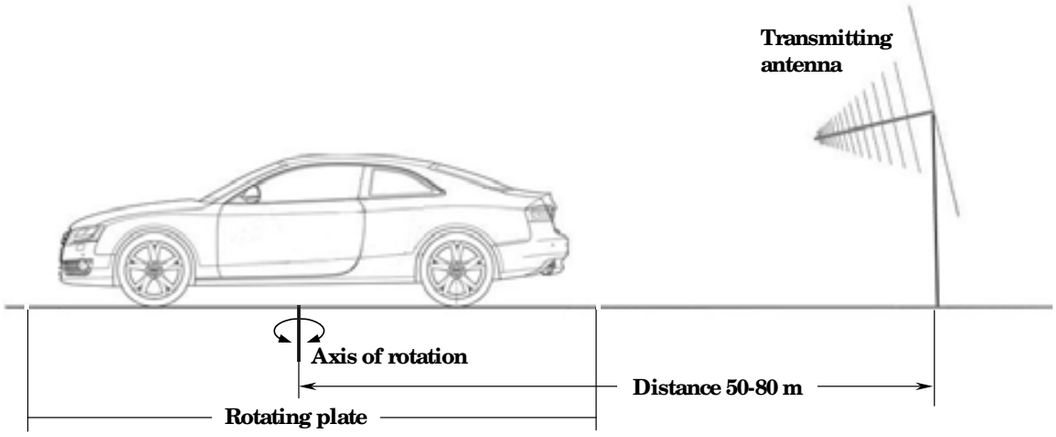

Fig. 23. Test setup for antenna pattern measurements

In the current example, reception of the glass antenna placed in a rear window of an AUDI A5 model is examined. An aim of the testing is to analyze the influence of different antenna amplifiers on the level of the received signal. First, a passive antenna is analyzed, and then five different amplifiers, one after another, are connected to the antenna to compare the received voltages. The simulations are done at selected frequencies in FM and DAB/ TV (band III) ranges. To obtain vertical and horizontal components of the far-field antenna patterns, excitation of the transmitting antenna is replaced by vertically and horizontally polarized plane waves with equivalent magnitudes. The elevation angle of the incident plane wave corresponds to the location of the transmitting antenna (Fig. 23) and is $\theta = 85°$. Instead of rotating the car, in simulation model it is possible to vary the azimuth angle ϕ from 0° to 360° to obtain the received signal as a function of azimuth angle. In a given example, angle ϕ varies from 0° to 350° with a step of 10° (Fig. 24). One set of vertically polarized waves and one with horizontal polarization gives a total of 72 incident plane waves. A multi-excitation technique is used to effectively perform these simulations.

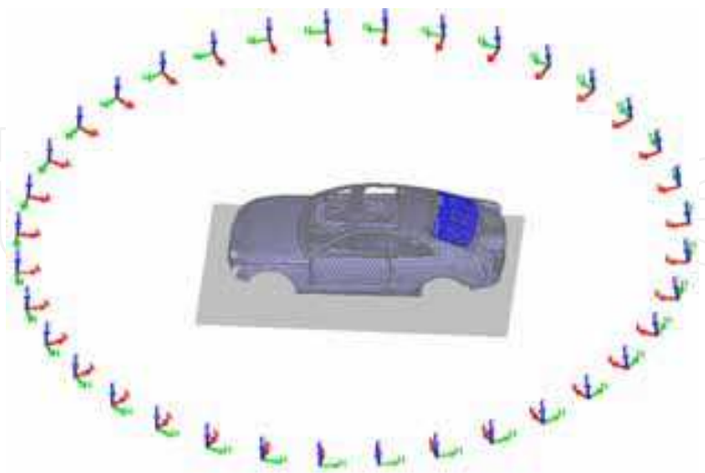

Fig. 24. A Car body exposed by plane waves incident from different angles

To consider different amplifiers, a multi-partitioned technique is also used. Amplifiers are included in a simulation model as 2-port networks with measured S-parameters, see Fig. 25 a) to e), and applied to the pigtail wire connected to the antenna structure. In multi-

partitioned calculations, the car body and the complete glass antenna (Fig. 26), except of the pigtail wire connected to the antenna, are defined as the basis part. While 6 copies of the pigtail wire are defined as additional parts: 5 for active antenna with different amplifiers (Fig. 27), 1 with non-radiating 3-cm TL element with 50-Ohm resistance for passive antenna.

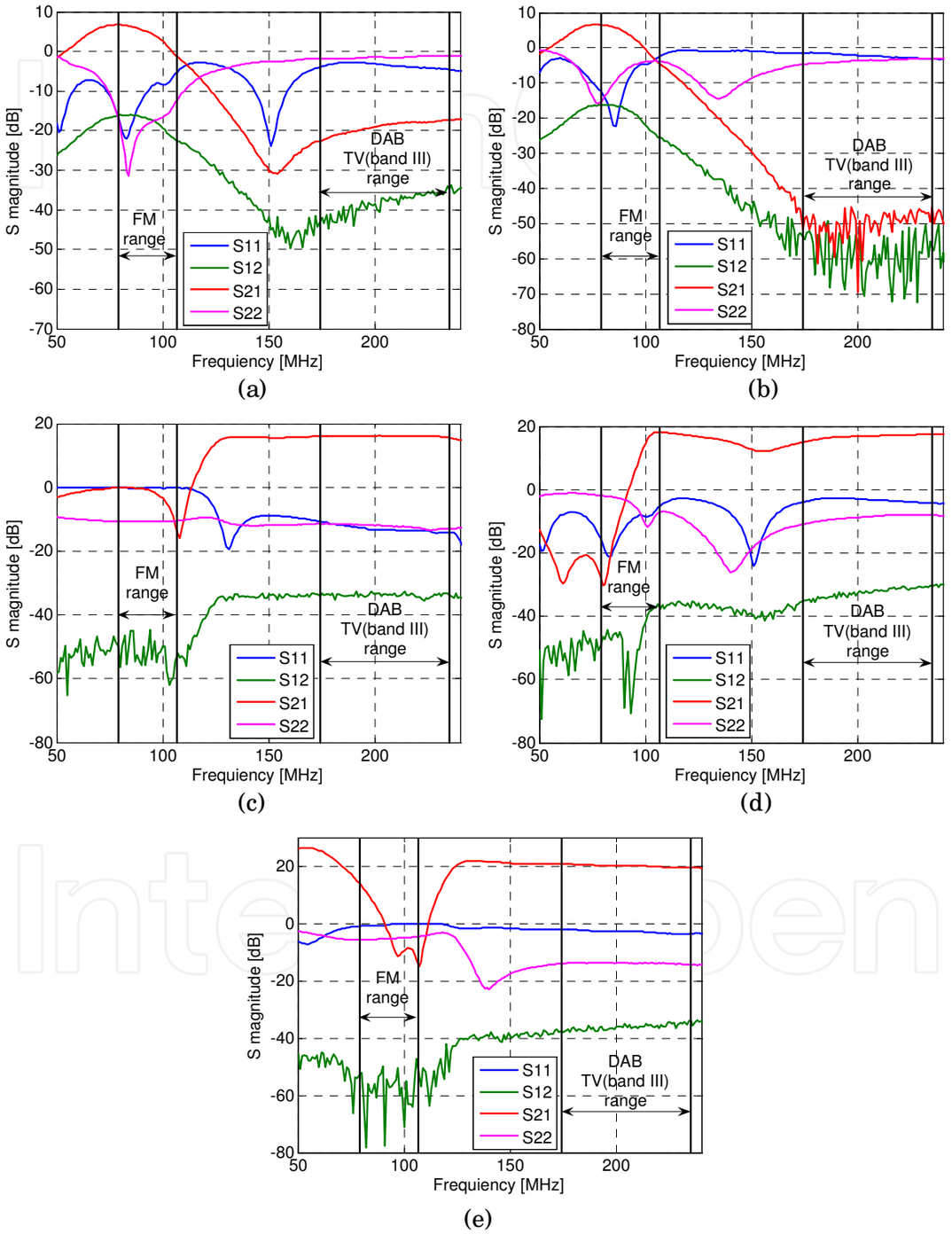

Fig. 25. Measured S-parameters of RF amplifiers as a function of frequency: a) AM/ FM1 amplifier, b) FM2 amplifier, c) DAB amplifier, d) TV1 amplifier, e) TV3 amplifier

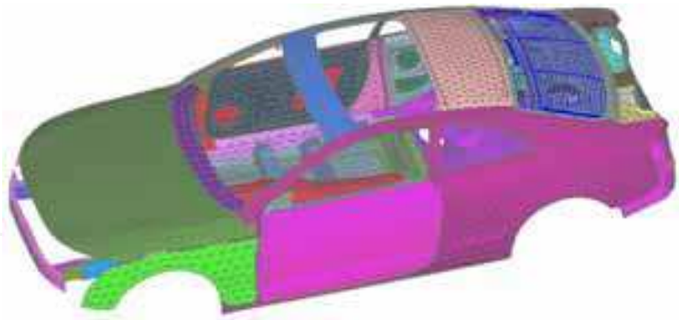

Fig. 26. A car model with a complete antenna pattern considered as a basis part

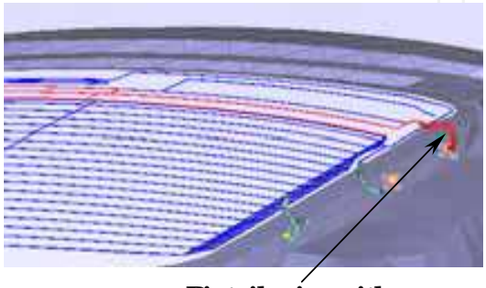

Fig. 27. Pigtail wire copies with different amplifiers (partitions)

Fig. 28 shows calculated voltages received by the antenna with different amplifiers at a certain frequency f = 174 MHz as a function of azimuth angle ϕ of incident plane wave for vertical and horizontal polarizations. A received voltage for the passive antenna is considered as a reference to show the effect of the amplifier. Besides, Figs. 29 and 30 show the frequency dependencies of the averaged received voltages (over ϕ angle) for the different frequency ranges and polarizations of incident plane wave.

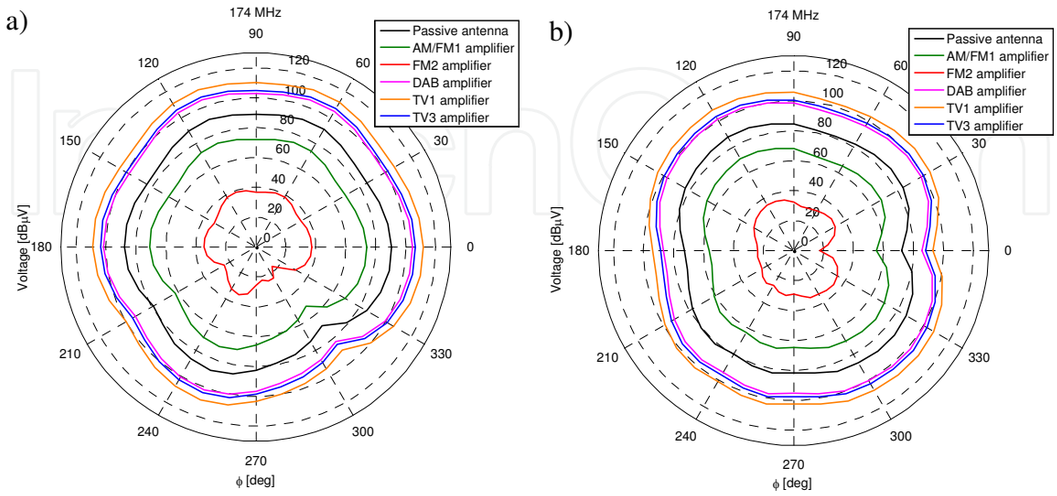

Fig. 28. Voltage received by antenna with different amplifiers as a function of azimuth angle of plane wave at a frequency 174 MHz: a) vertical polarization, b) horizontal polarization

The presented results clearly show the effect of amplifiers. In the FM frequency range AM/ FM1 and FM2 amplifiers give a gain of 5-6 dB for both components, except of frequencies 100 MHz and 106.6 MHz, where the amplifier gain goes down. DAB, TV1 and TV3 amplifiers give a quite stable amplification of 15-20 dB in a complete DAB/ TV (band III) range. While this may seem to be a rather trivial result, it is quite important to be able to assess the actual gain of the amplifier in the complex environment of a complete vehicle, where the many installed antennas and amplifiers are strongly coupled.

Comparison of CPU times for the direct and multi-partitioned approach, both using the multi-excitation regime (Table 4), shows the 3.5 gain in calculation time for 6 partitions. This demonstrates the efficiency of the multi-partitioned scheme for vehicle antenna problems.

Solution type	CPU time for a one frequency point
Direct solution with multi-excitation (6 tasks; 72 excitation sources)	9.84 hours (1.64 hours per task)
Matrix Partitioning with multi-excitation (6 partitions; 72 excitation sources)	2.85 hours (2 hours for basis + 0.85 hours for 6 partitions; 8.5 minutes for each partition)

Table 4. Summary of computational times

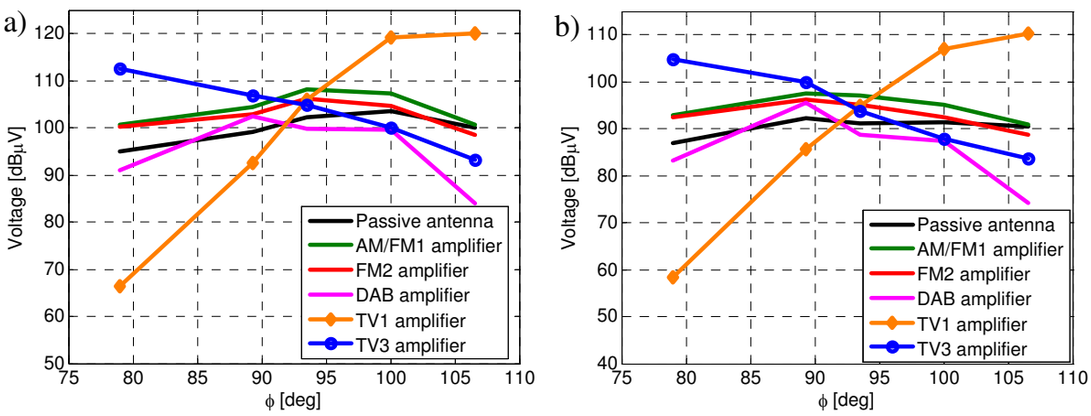

Fig. 29. Averaged received voltage in FM frequency range:
a) vertical component, b) horizontal component

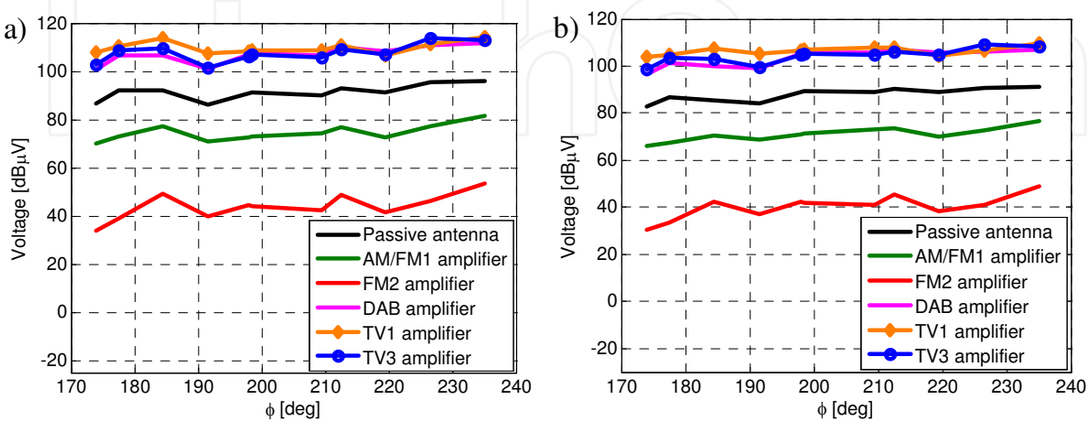

Fig. 30. Averaged received voltage in DAB/ TV (band III) frequency range:
a) vertical component, b) horizontal component

8. Conclusion

Modern automotive antenna simulations represent a sophisticated process that requires development of the new computational methods and techniques. When these methods are applied, the overall design process can be speed up considerably. In this chapter, a number of recent developments in this area have been described, which are based on the enhancements of the traditional MoM scheme. A special attention has been devoted to the adaptive and hybrid methods, special Green's functions for conformal glass antennas, and optimization techniques. Validation and application examples have been considered along with supplied experimental data. The benefits of the described new computational methods and techniques have been illustrated. It has been shown that the combined usage of traditional and special methods and techniques described in this chapter facilitates obtaining the accurate and optimal solution of complicated automotive antenna problems.

9. References

Ala, G. & Di Silvestre, M.L. (2002). A simulation model for electromagnetic transients in lightning protection systems. *IEEE Transactions on Electromagnetic Compatibility*, Vol. 44, No. 4, November 2002, pp. 539-554.

Bogdanov, F.G. & Jobava, R.G. (2003). Examination of boundary conditions performance for estimating accuracy of MoM solutions on square plate benchmark geometry using triangle doublet basis functions. *Microwave and Optical Technology Letters*, Vol. 39, No. 3, November 2003, pp. 193-196.

Bogdanov, F.G.; Jobava, R.G. & Frei, S. (2004a). Scheme of improving accuracy of MoM solutions based on analysing boundary conditions performance, *Proceedings of the 2004 East-West Workshop, Advance Techniques in Electrodynamics*, pp. 217-224, Warszawa, Poland May 2004.

Bogdanov, F.G.; Jobava, R.G. & Frei, S. (2004b). Estimating accuracy of MOM solutions on arbitrary triangulated 3-D geometries based on examination of boundary conditions performance and accurate derivation of scattered fields. *Journal of Electromagnetic Waves and Applications*, Vol. 18, No. 7, 2004, pp. 879-897.

Bogdanov, F.G.; Jobava, R.G.; Gheonjian, A.L.; Yavolovskaya, E.A.; Bondarenko, N.G. & Injgia T.N. (2009). Development and application of an enhanced MoM scheme with integrated generalized N-Port networks. *PIERM 07*, pp. 135-148.

Bogdanov, F.G.; Karkashadze, D.D.; Jobava, R.G.; Gheonjian, A.L.; Yavolovskaya, E.A. & Bondarenko, N.G. (2010a). Advantage of a hybrid MoM scheme with approximate Green function to model integrated glass antennas, *Microwave and Optical Technology Letters*, Vol. 52, No. 2, February 2010, pp. 351-354.

Bogdanov, F.G.; Karkashadze, D.D.; Jobava, R.G.; Gheonjian, A.L.; Yavolovskaya, E.A.; Bondarenko, N.G. & Ullrich, C. (2010b). Validation of hybrid MoM scheme with included equivalent glass antenna model for handling automotive EMC problems. *IEEE Transactions on Electromagnetic Compatibility*, Vol. 52, No. 1, 2010, pp. 164-172.

Bogdanov, F.G.; Jobava, R.G. & Tsereteli, P. (2010c). TriD: Tri-Dimensional code for electromagnetic modeling of arbitrary surface and wire configurations. User's Manual. Version 5.08, EMCoS, Tbilisi.

EMCoS (2010a): EMC Studio, http:/ / www.emcos.com

EMCoS (2010b): EMCoS Antenna VirtualLab, http:/ / www.emcos.com

Erteza, A. & Park, B.K. (1969). Nonuniqueness of resolution of Hertz vector in presence of a boundary, and a horizontal dipole problem. *IEEE Transactions on Antennas and Propagation,* Vol. AP-17, May 1969, pp. 376-378.

Jobava, R.; Bogdanov F.G.; Gheonjian, A. & Frei, S. (2005). Application of adaptive scheme for the method of moments in EMC automotive problems, *Proceedings of the 16th International Zurich Symposium on Electromagnetic Compatibility*, pp. 131-136, Zurich, Switzerland, February 2005.

Harrington, R.F. (1968). Field Computation by Moment Methods, *Macmillan Publishing Company*, New York.

Harrington, R.F. & Mautz, J.R. (1975). An impedance sheet approximation for thin dielectric shells. *IEEE Trans. Antennas and Propagation*, Vol. 23, No. 4, July 1975, pp. 531-534.

Miller, E.K.; Poggio, A.J; Burke, G.J. & Selden, E.S. (1972a). Analysis of wire antennas in the presence of a conducting half-space: Part I. The vertical antenna in free space. *Canadian Journal of Physics*, Vol. 50, 1972, pp. 879-888.

Sommerfeld, A. (1949). Partial Differential Equations in Physics. New York: Academic Press.

Su, D.Y.; Fu, D.-M. & Chen, Z.-H. (2008). Numerical modeling of active devices characterized by measured S-parameters in FDTD, *Progress in Electromagnetics Research*, PIER 80, 2008, pp. 381-392.

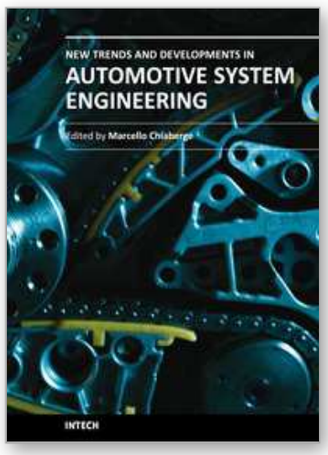

New Trends and Developments in Automotive System Engineering
Edited by Prof. Marcello Chiaberge

ISBN 978-953-307-517-4
Hard cover, 664 pages
Publisher InTech
Published online 08, January, 2011
Published in print edition January, 2011

In the last few years the automobile design process is required to become more responsible and responsibly related to environmental needs. Basing the automotive design not only on the appearance, the visual appearance of the vehicle needs to be thought together and deeply integrated with the â€œpowerâ€ developed by the engine. The purpose of this book is to try to present the new technologies development scenario, and not to give any indication about the direction that should be given to the research in this complex and multi-disciplinary challenging field.

How to reference
In order to correctly reference this scholarly work, feel free to copy and paste the following:

Faik Bogdanov, Roman Jobava, David Karkashadze, Paata Tsereteli, Anna Gheonjian, Ekaterina Yavolovskaya, Detlef Schleicher, Christoph Ullrich and Hicham Tazi (2011). Computational Techniques for Automotive Antenna Simulations, New Trends and Developments in Automotive System Engineering, Prof. Marcello Chiaberge (Ed.), ISBN: 978-953-307-517-4, InTech, Available from: http://www.intechopen.com/books/new-trends-and-developments-in-automotive-system-engineering/computational-techniques-for-automotive-antenna-simulations

INTECH
open science | open minds

InTech Europe
University Campus STeP Ri
Slavka Krautzeka 83/A
51000 Rijeka, Croatia
Phone: +385 (51) 770 447
Fax: +385 (51) 686 166
www.intechopen.com

InTech China
Unit 405, Office Block, Hotel Equatorial Shanghai
No.65, Yan An Road (West), Shanghai, 200040, China
中国上海市延安西路65号上海国际贵都大饭店办公楼405单元
Phone: +86-21-62489820
Fax: +86-21-62489821

IntechOpen